HIGH POWER LASER
SCIENCE AND ENGINEERING

RESEARCH ARTICLE

Nanosecond laser conditioning of multilayer dielectric gratings for picosecond–petawatt laser systems

Kun Shuai[1,2,3], Yuanan Zhao[1,2,3], Xiaofeng Liu[1,2,3], Xiangkun Lin[1,2,3], Zhilin Xia[4], Keqiang Qiu[5], Dawei Li[1,3], He Gong[1,6], Yan Zhou[1,6], Jian Sun[1,3], Li Zhou[7], Youen Jiang[7], Yaping Dai[8], and Jianda Shao[1,3,9]

[1] *Laboratory of Thin Film Optics, Shanghai Institute of Optics and Fine Mechanics, Chinese Academy of Sciences (CAS), Shanghai, China*

[2] *Center of Materials Science and Optoelectronics Engineering, University of Chinese Academy of Sciences, Beijing, China*

[3] *Key Laboratory of Materials for High Power Laser, Chinese Academy of Sciences, Shanghai, China*

[4] *School of Materials Science and Engineering, Wuhan University of Technology, Wuhan, China*

[5] *National Synchrotron Radiation Laboratory, University of Science and Technology of China, Hefei, China*

[6] *School of Optical-Electrical and Computer Engineering, University of Shanghai for Science and Technology, Shanghai, China*

[7] *National Laboratory on High Power Laser and Physics, Shanghai Institute of Optics and Fine Mechanics, CAS, Shanghai, China*

[8] *Research Center of Laser Fusion, China Academy of Engineering Physics, Mianyang, China*

[9] *Hangzhou Institute for Advanced Study, University of Chinese Academy of Sciences, Hangzhou, China*

(Received 27 June 2023; revised 18 August 2023; accepted 7 September 2023)

Abstract

Multilayer dielectric gratings (MLDGs) are crucial for pulse compression in picosecond–petawatt laser systems. Bulged nodular defects, embedded in coating stacks during multilayer deposition, influence the lithographic process and performance of the final MLDG products. In this study, the integration of nanosecond laser conditioning (NLC) into different manufacturing stages of MLDGs was proposed for the first time on multilayer dielectric films (MLDFs) and final grating products to improve laser-induced damage performance. The results suggest that the remaining nodular ejection pits introduced by the two protocols exhibit a high nanosecond laser damage resistance, which remains stable when the irradiated laser fluence is more than twice the nanosecond-laser-induced damage threshold (nanosecond-LIDT) of the unconditioned MLDGs. Furthermore, the picosecond-LIDT of the nodular ejection pit conditioned on the MLDFs was approximately 40% higher than that of the nodular defects, and the loss of the grating structure surrounding the nodular defects was avoided. Therefore, NLC is an effective strategy for improving the laser damage resistance of MLDGs.

Keywords: laser-induced damage threshold; multilayer dielectric gratings; nanosecond laser conditioning; nodular defects; picosecond–petawatt laser systems

1. Introduction

High-energy petawatt laser systems (HPLSs)[1–4] have unparalleled application in inertial confinement fusion[5], laboratory extreme physics research[6] and laser-accelerated particle beams[7,8]. Chirped pulse amplification (CPA)[9,10] technology has been utilized to achieve ultra-high-intensity pulse outputs in HPLSs. The laser-induced damage threshold (LIDT) of a multilayer dielectric grating (MLDG), which is a key optical component of the CPA system, directly determines the final output capacity of the entire system. Since MLDGs were proposed, the quest for more robust MLDGs has promoted the investigation of their laser damage resistance enhancement and laser-induced damage mechanisms.

The first investigations on LIDT enhancement of MLDGs were reported in 1996[11]. Although some benefits were obtained by optimizing the ion-beam etching manufacturing process[12], the electric-field intensity (EFI) enhancement introduced by the surface-relief grating structure was unavoidable, and the LIDT exhibited a strong dependence on the EFI. Because the initial damage of MLDGs

---

1
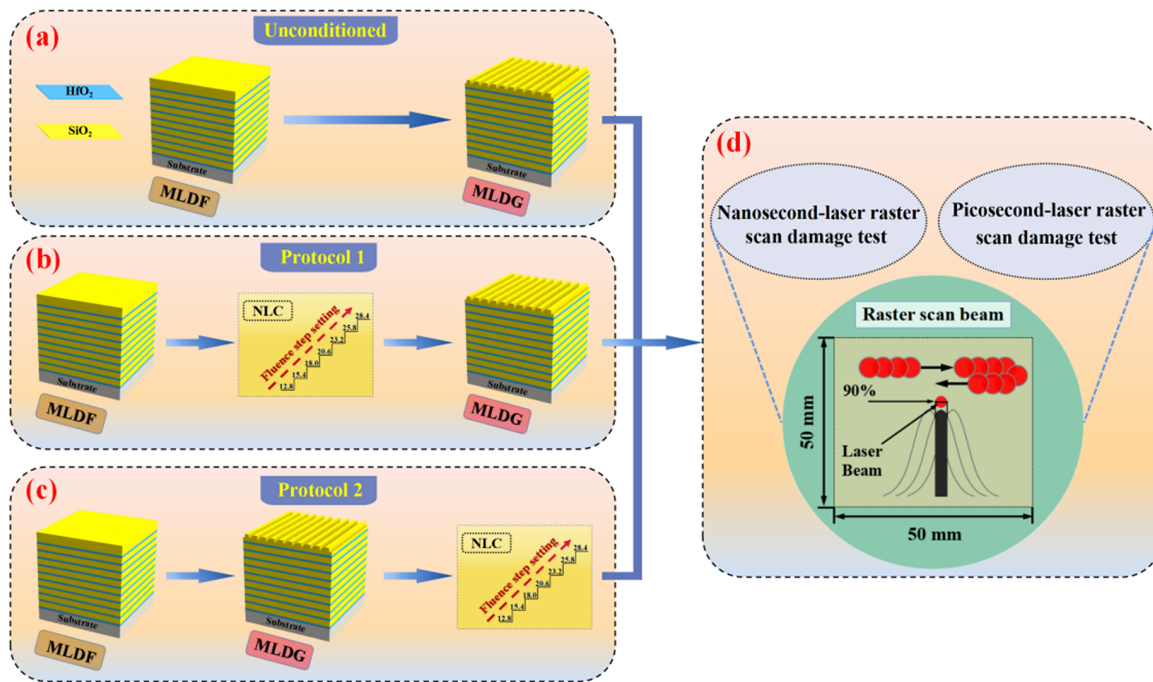
Figure 1. Schematic representation of the nanosecond and picosecond laser damage tests performed on three types of MLDG samples: (a) unconditioned MLDG, (b) MLDF conditioning and (c) MLDG conditioning. (d) Schematic of the raster scan damage tests.

induced by a ultrashort pulse is directly related to the EFI distribution[13,14], theoretical optimization of the near field in MLDGs has become the focus of several studies[13–16]. The EFI enhancement can be decreased by increasing the incident angle[12] and using a thin pillar profile[15]. Xie *et al.*[16] manufactured a rectangular MLDG profile to further reduce the EFI in the grating pillar. In addition, surface contaminants, including photoresists, etch residues and surface debris, are well-known reasons for reducing the laser damage resistance[17–19]. Developing advanced cleaning methods, such as dilute-buffered hydrofluoric acid solution cleaning[20] and low-temperature chemical cleaning[21], can improve the laser damage resistance of MLDGs. Recently, these contaminants have been shown to extend to a 50–80-nm layer below the surface[22].

Efforts have been devoted to minimizing the peak EFI and reducing the subsurface contamination produced during MLDG fabrication[22,23]. However, potential defects, especially nodular defects in multilayer coating stacks[24], primarily limit the laser damage resistance of MLDGs exposed to nanosecond and picosecond laser irradiation[25–29]. Moreover, the presence of nodules results in the absence of a grating structure around the bulge area[30]. These factors necessitate the removal of nodular defects. Based on the successful application of laser conditioning in high reflectors and polarizers[31–38], we first propose removal of nodular defects in MLDGs through nanosecond laser conditioning (NLC). Since the nodular defects are deposited during the preparation of multilayer dielectric films (MLDFs), the appropriate process stage for performing NLC needs to be

identified. If NLC is performed before the surface-relief grating structure is fabricated (on the MLDF), then the pits and scalding regions induced by the MLDF conditioning may affect the subsequent lithography process. However, if the NLC is performed on the final grating products, can the effect of nodule removal on the surface-relief grating structure be tolerated?

In this study, two options for integrating NLC into the MLDG fabrication process were introduced to remove nodular defects. The NLC was applied to the MLDFs (Protocol 1) and final MLDGs (Protocol 2), as shown in Figures 1(b) and 1(c). We first investigated the effects of the nodular ejection pits formed in these two protocols and simulated their electric-field distributions using the finite element method (FEM). Subsequently, the morphological characteristics of the plasma-scalding regions that appeared in the two protocols were compared. Finally, nanosecond and picosecond laser raster scan damage tests were performed on the unconditioned and conditioned MLDGs to evaluate the overall effects of these two conditioning protocols. A maximum improvement of approximately 40% was observed in the picosecond-LIDT of the MLDGs after the removal of the nodular defects.

2. Sample and experimental protocols

MLDFs were deposited with alternating HfO_2/SiO_2 layers on a 50 mm × 50 mm × 1.5 mm fused silica substrate by electron beam evaporation. The basic stack formula[39] of the multilayer film is based on $(H2L)^k$, where H and L

represent quarter-wave optical thickness layers of HfO_2 and SiO_2, respectively. Subsequently, the MLDFs were subjected to photoresist spin-coating, exposure, photoresist development, etching and cleaning to obtain the final MLDGs. The MLDGs were designed with a groove density of 1740 lines/mm, which could provide a –1st-order diffraction efficiency of more than 97% at an incidence of 67° in a transverse electric (TE) polarized laser with a wavelength of 1064 nm[30].

The NLC process was introduced to the MLDF (Protocol 1) and final MLDG (Protocol 2), as shown in Figures 1(b) and 1(c), respectively. Subsequently, nanosecond and picosecond laser damage experiments were performed on the unconditioned and conditioned MLDGs to evaluate and compare their laser damage resistances. The raster scanning method[30] was applied in the NLC and laser damage experiments, and the distance between the neighboring test sites was equal to the diameter of the beam at 90% of the peak fluence, as shown in Figure 1(d). The laser scanning speed was set to approximately 8.3 mm/s with a laser repetition rate of 30 Hz.

The NLC and nanosecond laser experiments were performed using a 1064 nm neodymium-doped yttrium aluminum garnet (Nd:YAG) laser at an incidence of 67° in the TE polarization mode, as described in Ref. [30]. The nanosecond laser pulse width was approximately 8.0 ns, and the waist radius of the Gaussian beam at a normal incidence was approximately 0.6 mm. During the NLC process, the fluence of the incident laser was gradually increased from 12.8 to 28.4 J/cm^2, which was higher than the nanosecond-LIDTs of the samples. This was expected to remove nodular defects effectively and cause negligible and benign damage.

The picosecond laser damage apparatus is described in Refs. [40,41]. The incident laser was operated at a central wavelength of 1053 nm with an incident angle of 67° in the TE polarization mode. The picosecond laser pulse width was approximately 8.6 ps, and the waist radius of the focused beam was approximately 48.9 μm. During the picosecond laser damage experiment, the regions where the nodular defects and nodular ejection pits were generated by Protocols 1 and 2 were raster-scanned for comparison.

The LIDT is defined as the maximum fluence at which no damage occurs. The laser fluence used in this study was provided as the beam normal. The damage density measured as a function of the laser fluence was defined as the number of damage sites per scanning area (1 cm^2 for the raster scan in the final nanosecond laser damage tests).

Optical microscopy (OM, Olympus BX53M) and focused ion-beam scanning electron microscopy (FIB-SEM, Zeiss Auriga) were used to characterize the morphological evolution after conditioning, photoresist spin-coating and cleaning in Protocol 1, as well as to evaluate the effects of the byproducts of the two protocols on the morphology of the grating surface. Finally, the laser damage resistance of the MLDGs

conditioned by these two protocols was compared under a gradually increasing incident laser fluence.

3. Morphological comparison and analysis

NLC with nodular defects introduced two typical byproducts (nodular ejection pits and plasma-scalding regions) in the final MLDGs. We first tracked the morphological characteristics of the nodular ejection pits generated in Protocol 1 at different preparation stages. The effects of the two byproducts generated by these two protocols on the surface morphology of the MLDG were analyzed and compared.
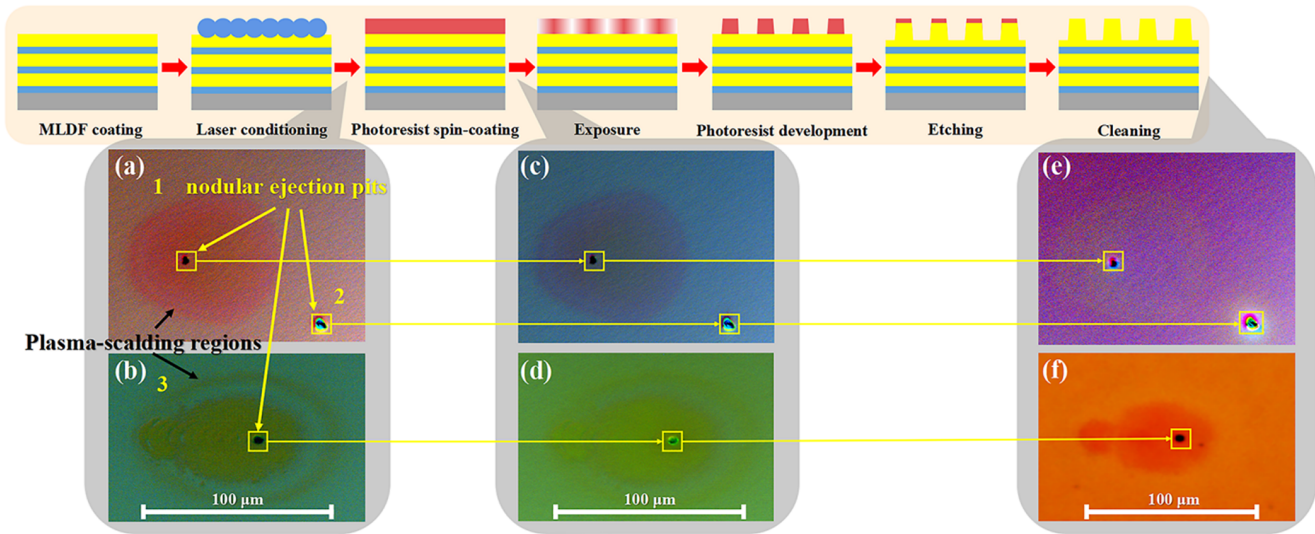
3.1. Nodular ejection pits

Figure 2 shows the surface morphologies of the nodular ejection regions after the MLDF conditioning, spin-coating and MLDG cleaning in Protocol 1. The nodular ejection pits marked as 1 and 3 in Figures 2(a) and 2(b), respectively, are accompanied by discolored plasma scalds, whereas the position marked as 2 in Figure 2(a) represents a nodular ejection pit without a scald. Figures 2(c)–2(f) show that the nodular ejection pits and plasma scalds remain the same after the photoresist spin-coating and MLDG cleaning processes, respectively. Thus, the morphological modifications introduced by Protocol 1 exhibit replication characteristics at the subsequent process stages, and OM analyses reveal that these replication characteristics do not seem to affect the subsequent preparation process of the MLDG.

Further morphological characterization was performed using scanning electron microscopy (SEM). Figure 3(a) shows the typical surface morphology of a nodular defect in the MLDF, which has an evident bulge structure. Figures 3(b)–3(d) display the morphological characteristics corresponding to the nodular ejection pits after the MLDF conditioning, photoresist spin-coating and MLDG cleaning, respectively. The results indicate that the pit is filled with photoresist after the spin-coating, and the multilayer structure in the pit cannot be observed, as shown in Figure 3(c). After cleaning, the internal structure of the pit was reproduced, and the grating relief structure was etched in the area around the pit, as shown in Figure 3(d).

The bulging nodular defect results in the absence of grating structures in the surrounding annular area, as shown in Figure 4(a), because of the presence of nodular defects, which affect the distribution of the surrounding exposure field during the exposure stage of the MLDG fabrication. After removing the nodule, as in Protocol 1, the nodular ejection pit in the MLDG exhibits a small affected area with a tightly surrounding grating structure, as shown in Figure 4(b). However, Protocol 2 cannot prevent the disappearance of grating structures around the nodular ejection pit, as shown in Figure 4(c). The square of EFI enhancement
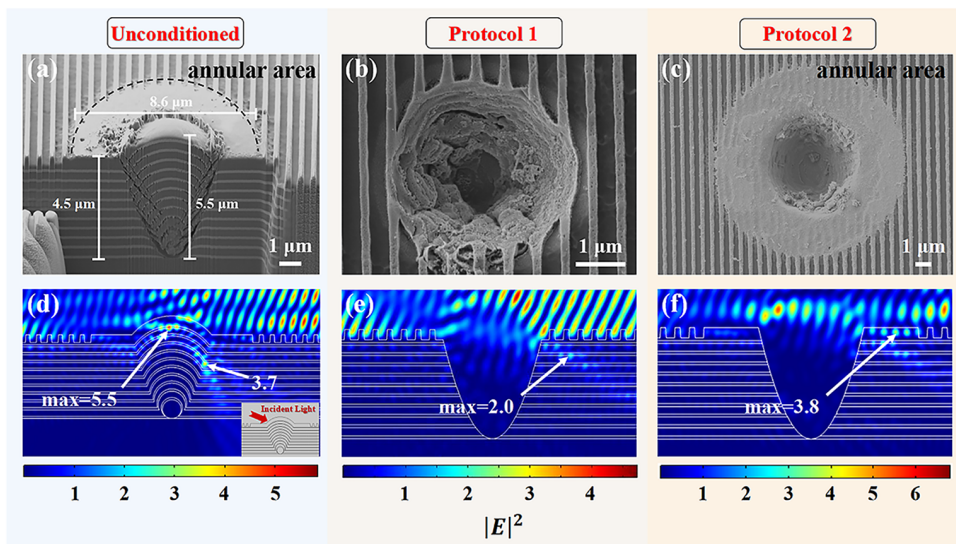
Figure 2. OM images of the nodular ejection pits and plasma scalds originating from Protocol 1. (a), (b) Before photoresist spin-coating after MLDF conditioning. (c), (d) After photoresist spin-coating. (e), (f) After MLDG cleaning.
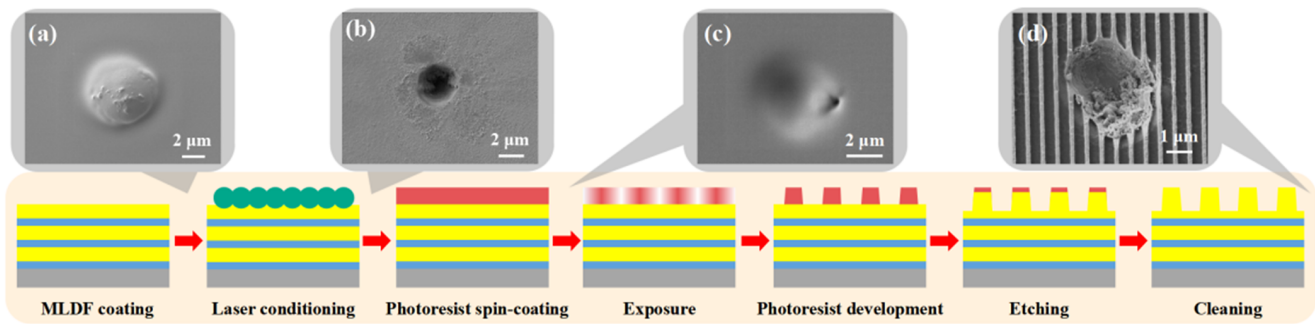
Figure 3. SEM images of the nodular defect and ejection pits at the different MLDG fabrication stages. (a) Typical bulged nodular defect in the MLDF and (b)–(d) morphologies of the nodular ejection pits after the MLDF conditioning, photoresist spin-coating and grating cleaning, respectively.

Figure 4. (a) Typical cross-sectional morphology of a nodular defect in the unconditioned MLDG. (b), (c) SEM images of the typical nodular ejection pits caused by Protocols 1 and 2, respectively. (d)–(f) Simulated $\left|E^2\right|$ distributions corresponding to the morphological structures in (a)–(c), respectively.

Table 1. Model parameters used in the calculations.

Parameter	d	t	n_L	n_H	Wavelength	Incidence	Polarization
Value	1 μm	4.5 μm	1.453	1.962	1064 nm	67°	TE

Note: n_L and n_H represent the refractive indices of SiO_2 and HfO_2, respectively.

$(|E^2|)$ distributions of the nodular defects and nodular ejection pits were simulated using the FEM. A 2D simulation model with periodic boundaries on the left- and right-hand sides was used to reduce the computation. The simulation domain was 100 μm wide and 7.5 μm high for nodular defects and nodular pits initiating from the 1 μm seeds. The geometry of the nodular defect can be expressed as $D = \text{sqrt}\,(4dt)$[42], where D is the nodule diameter, d is the diameter of the nodular seed and t is the seed depth. Table 1 lists the model parameters used in the calculations.

The parabolic structure generated by the nodular ejection is reset as an air domain, and only the annular areas around the pits generated by Protocols 1 and 2 are different. Figure 4(d) shows the $|E^2|$ distributions of the bulged nodular defect, and Figures 4(e) and 4(f) depict the two typical nodular ejection pits caused by Protocols 1 and 2, respectively. The maximum $|E^2|$ of the nodular defect (= 5.5) is observed in the dome film at the top of the defect, as shown in Figure 4(d). In addition, a strong $|E^2|$ (= 3.7) is detected at the right-hand boundary between the nodule and the holonomic layer. For the nodular ejection pits, the maximum $|E^2|$ in the pits generated by Protocols 1 and 2 decreases to 2.0 and 3.8, respectively, as shown in Figures 4(e) and 4(f). This result indicates that the laser damage resistance of the nodular ejection pits seems to be higher than that of the nodular defects, especially that of the pits generated in Protocol 1.
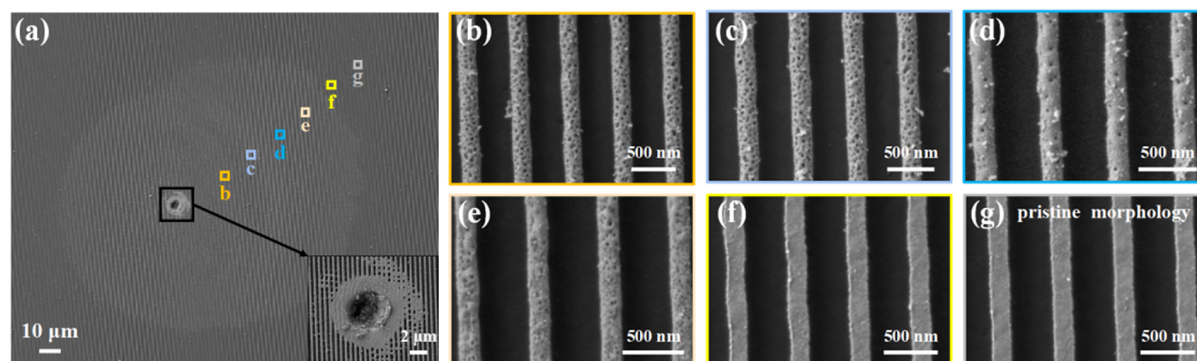
3.2. Plasma-scalding regions

The effects of the plasma scalds, induced by the two protocols, on the final grating structure were evaluated. Figure 5(a) presents the typical morphology of a plasma-scalding region, with two elliptical structures and a bright nodular ejection pit, induced by Protocol 1. Six positions outside the center of the pit were selected for comparison. Figures 5(b)–5(g) present the local magnified images of the positions marked by rectangles in Figure 5(a). For comparison, the pristine surface is also displayed in Figure 5(g), which shows a clear boundary between the pillars and grooves. In the elliptical plasma-scalding region, some molten holes are visible on the surface of the pillars, particularly at the edges of the two ellipses, marked as c and e. In addition, the grating grooves, shown in Figures 5(c) and 5(e), exhibit some 'wavy' features, possibly due to the relatively severe scald; by contrast, this feature is not noticeable in the grating grooves at the positions marked as b and d. At the outside point f, which is near the outer edge of the plasma-scalding region, the pillars and grooves are not affected, and the surface morphology is consistent with that of the primitive surface shown in Figure 5(g).

The typical morphological characteristics of the bright plasma-scalding region with a nodular ejection pit induced by Protocol 2 are shown in Figure 6(a). Figures 6(b)–6(g) show the local magnified SEM images of the six positions marked by rectangles (in color) in Figure 6(a). However, in contrast to the morphology induced by Protocol 1, in the case of Protocol 2, more molten holes are concentrated on the pillar surface, especially at the positions near the ejection pit, marked by b and c. Furthermore, although many ejection residues also adhere to the surface of the grating pillars, the grating grooves are not modified, and their surfaces are smooth. At position f outside the scalding region, the morphological characteristics of the pillars are almost the same as those of the pristine surface of the MLDGs, as shown in Figures 6(f) and 6(g), similar to Protocol 1.
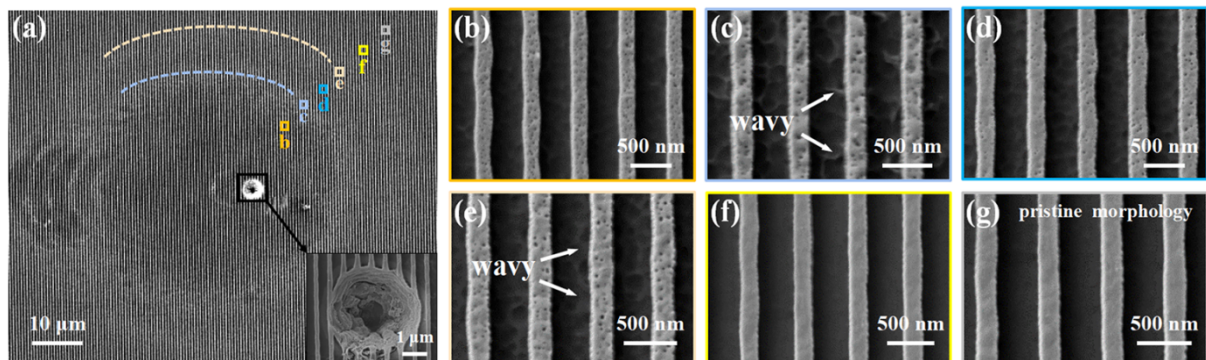
Figure 5. (a) SEM image of the plasma-scalding region induced by the NLC in Protocol 1; the inset image shows a local magnified view of the nodular ejection pit. (b)−(g) Local magnified SEM images of the positions marked by rectangles (in color) in (a).

Figure 6. (a) SEM image of the plasma-scalding region induced by the NLC in Protocol 2; the inset image indicates the local magnified view of the central nodular ejection pit. (b)−(g) Local magnified SEM images of the positions marked by rectangles (in color) in (a).

4. Laser damage results and discussion

### 4.1. Comparison of nanosecond laser damage performances

4.1.1. LIDT and damage density

The nanosecond-LIDTs and damage densities of the unconditioned and conditioned MLDGs are shown in Figures 7(a) and 7(b), respectively. The LIDT of the MLDGs conditioned by Protocol 1 and that of the unconditioned MLDGs are almost the same (15.4 J/cm^2), whereas that of the MLDGs conditioned by Protocol 2 is higher (18.0 J/cm^2). The damage density is calculated as the number of damaged sites in an area of 1 cm^2. Overall, the damage densities of the three types of samples increase with the laser fluence for different slopes. The damage densities of the MLDGs conditioned using Protocols 1 and 2 decrease, especially that of the latter. Figure 7(b) shows that when the irradiated laser fluence reaches 25.8 J/cm^2, the damage density of the unconditioned MLDGs is 73 cm^{-2}, whereas those of the MLDGs conditioned by Protocols 1 and 2 are 50 and 3 cm^{-2}, respectively.

4.1.2. Damage resistance of nodular ejection pits

The nanosecond laser damage resistance of the nodular ejection pits induced by the two NLC protocols was further evaluated. Figure 8(a) shows the pristine morphological modifications of the three nodular ejection pits caused by the NLC in Protocol 1. The morphological evolution of the pits was characterized under gradually increasing incident laser fluence, and the corresponding results are shown in Figures 8(b)–8(f). Even if new severely damaged modifications appear in the scanning area with no observable defects, the nodular ejection pit areas (marked by red lines) remain highly resistant to higher-fluence irradiation. This observation suggests that the nodular ejection pits induced by the NLC in Protocol 1 are stable and do not cause any catastrophic damage, even at a fluence of 38.8 J/cm^2, as shown in Figure 8(f).
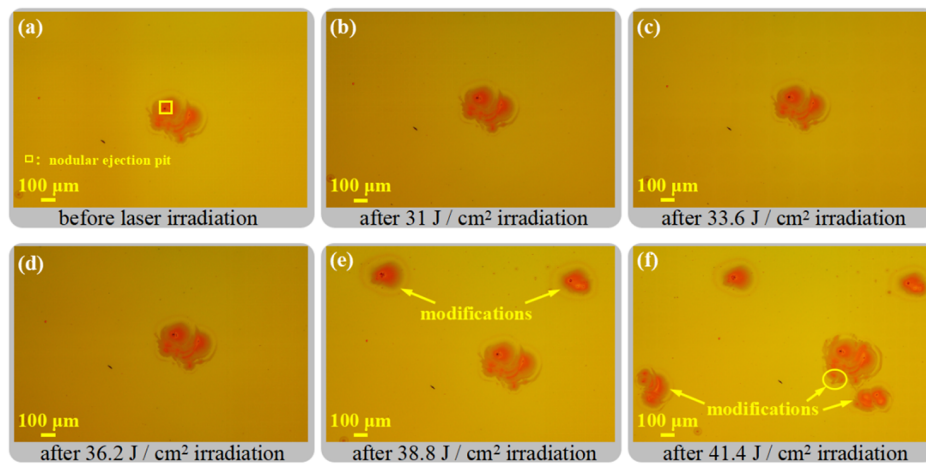
The morphological changes in a nodular ejection pit caused by the NLC in Protocol 2 were also tracked under gradually increasing incident laser fluences, and the results are displayed in Figures 9(a)–9(f). Similar to the pits in Protocol 1, the nodular ejection pit in Protocol 2 is highly
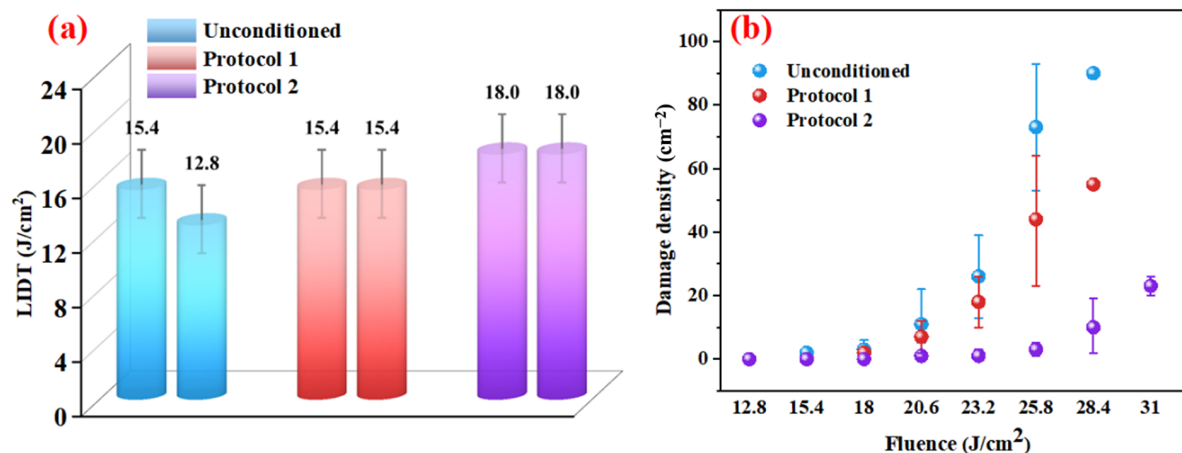
Figure 7. (a) LIDT results of the nanosecond laser raster scan; the two thresholds represent the results of two different test samples. (b) Damage density versus laser fluence (only the damage points that appear in the nanosecond laser damage test process are counted as damage).
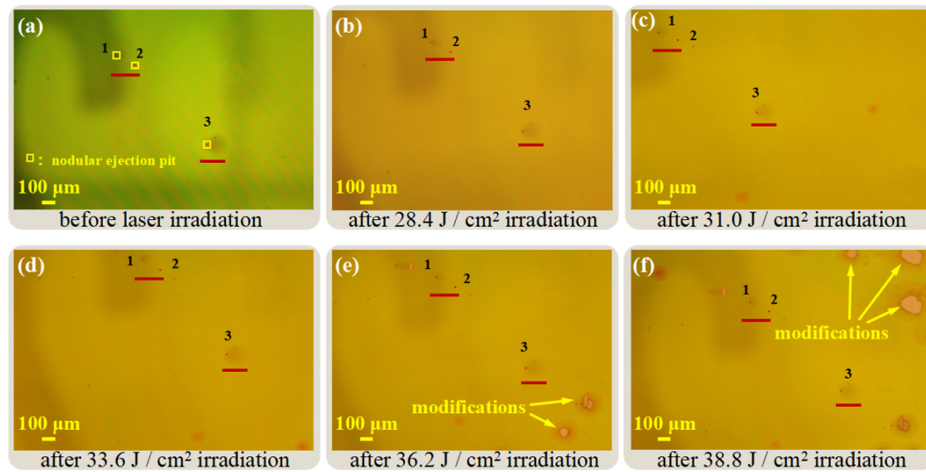
Figure 8. (a) OM image showing the pristine morphological modifications of the three nodular ejection pits induced by the NLC in Protocol 1. (b)–(f) OM images showing the morphologies of the ejection pit areas irradiated by gradually increasing nanosecond laser fluences; here, the red lines represent the nodular ejection pits on the MLDG.

Figure 9. (a) OM image showing the pristine morphological modifications of a nodular ejection pit induced by the NLC in Protocol 2. (b)–(f) Ejection pit region irradiated by gradually increasing nanosecond laser fluences.

stable under the irradiation of a laser fluence of 38.8 J/cm^2. When the laser fluence reaches 41.4 J/cm^2, noticeable modifications appear in the plasma-scalding area, as shown in Figure 9(f). Both pits caused by the two NLC protocols can withstand a laser fluence of 38.8 J/cm^2, which is higher than twice the LIDTs of the unconditioned MLDGs (15.4 and 12.8 J/cm^2) shown in Figure 7(a).

### 4.2. Comparison of picosecond laser damage performances

4.2.1. LIDT and damage morphology

The picosecond laser damage results of the nodular defects and nodular ejection pits caused by the NLC in Protocols 1 and 2 are displayed in Figure 10. The LIDT of the nodular defects is 2.0 J/cm^2, which is the lowest among those of the three sites. The LIDTs for the areas of the nodular ejection pits produced by Protocols 1 and 2 are 2.8 and

2.2 J/cm^2, respectively, which are approximately 40% and approximately 10% higher than those of the nodular defects.

The nodular defects are partially or completely ejected under a low laser fluence of 2.0 J/cm^2, while the surrounding grating pillars remain intact, as shown in Figures 11(a) and 11(d). This result indicates that these unstable nodular defects limit the LIDT of the MLDG. Figures 11(b) and 11(e) show that the nodular ejection pit in Protocol 1 remains intact under a laser fluence of 2.4 J/cm^2 and remains stable under a laser fluence of 3.2 J/cm^2, while catastrophic damage occurs in the surrounding pillars. The pillars near the ejection pit caused by Protocol 2 are more susceptible to damage than those caused by Protocol 1 and first fractured under a fluence of 2.2 J/cm^2, as shown in Figure 11(c). Figure 11(f) reveals that a laser fluence of 3.0 J/cm^2 damages almost all the pillars, and this damage may be attributed to the melting modification of the pillars in the plasma-scalding region, as shown in Figures 6(b) and 6(c).
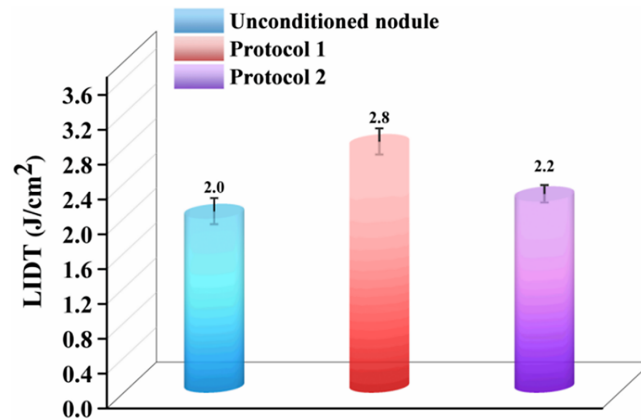
Figure 10. Picosecond-LIDTs of the unconditioned nodule and nodular ejection pits conditioned by Protocols 1 and 2.
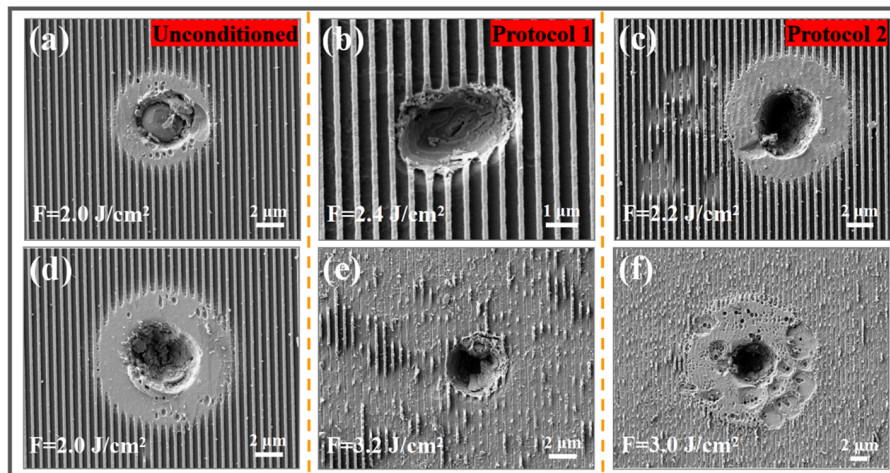
Figure 11. Typical morphological characteristics of the different test areas induced during the picosecond laser damage test. (a), (d) Unconditioned nodular defects. (b), (e) Nodular ejection pits caused by Protocol 1. (c), (f) Nodular ejection pits caused by Protocol 2 (where F denotes the incident laser fluence).
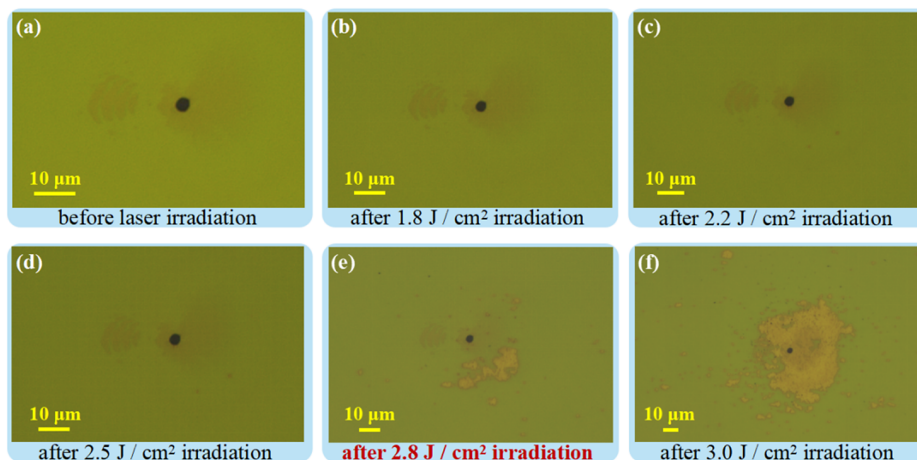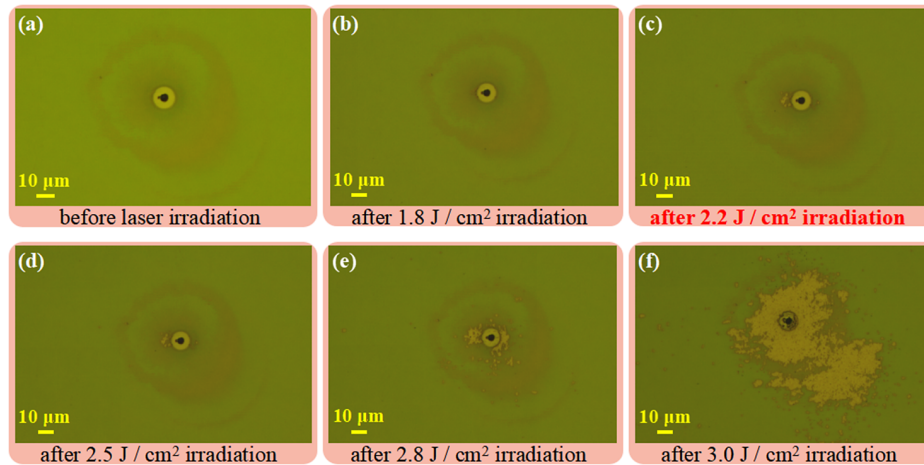

Figure 12. (a) OM image showing the pristine morphological modification of a nodular ejection pit in Protocol 1. (b)–(f) OM images showing the morphologies of the ejection pit area irradiated by the gradually increasing picosecond laser fluences.

4.2.2. Damage resistance of nodular ejection pits

The picosecond laser damage resistance of the two types of nodular ejection pits was evaluated by gradually increasing the laser fluence. Figures 12(b)–12(f) show the morphological evolution of the nodular ejection pit in the case of Protocol 1. When the laser fluence is 2.8 J/cm^2, the damage first occurs in the grating pillar area near the ejection pit, as shown in Figure 12(e). As the laser fluence

Figure 13. (a) OM image showing the pristine morphological modification of a nodular ejection pit in Protocol 2. (b)–(f) OM images showing the morphologies of the ejection pit area irradiated by the gradually increasing picosecond laser fluences.

increases to 3.0 J/cm^2, the initial damaged area surrounding the ejection pit expands further; however, the ejection pit remains stable, as shown in Figure 12(f).

Figure 13(a) shows an OM image of a pristine nodular ejection pit with an annular plasma-scalding area caused by Protocol 2. The morphological evolution of the pit irradiated by the gradually increasing picosecond laser fluence is shown in Figures 13(b)–13(f). Evidently, the damage first occurs in the plasma-scalding region on the left-hand side of the ejection pit at a low laser fluence of 2.2 J/cm^2, as shown in Figure 13(c). As the incident laser fluence is increased, the damaged area gradually expands. When the laser fluence reaches 3.0 J/cm^2, almost the entire plasma-scalding region is catastrophically damaged, which may be caused by a more serious modification of the region during the NLC process.

5. Conclusion

In this study, NLC, an effective method for removing nodular defects, was integrated into the different MLDG fabrication stages, that is, after the MLDF coating (Protocol 1) and cleaning (Protocol 2). Subsequently, nanosecond and picosecond laser raster scan damage tests were performed on the unconditioned and conditioned MLDGs for comparison.

Following the MLDF conditioning, the modifications caused by the nodular ejection pit and plasma scald exhibited morphological replication after the photoresist spin-coating and cleaning of the MLDG. Unlike bulging nodular defects, the ejection pits did not eliminate the surrounding grating structure. In addition, the remaining nodular ejection pits introduced by the two protocols exhibited a high nanosecond laser stability and remained stable even when the irradiated laser fluence was more than twice the nanosecond-LIDTs of the unconditioned MLDGs. The picosecond-LIDT of the nodular ejection pits produced by the MLDF conditioning was approximately 40% higher than that of the nodular defects, whereas the LIDT of the nodular ejection pit produced by the MLDG conditioning increased by only approximately 10% owing to the melting modification of the plasma-scalding region around the pit during the NLC process. Both protocols can remove nodular defects to improve the laser damage performance of MLDGs.

Laser conditioning performed using nanosecond pulses is universal and can be easily integrated, because a vacuum environment to prevent nonlinear self-focusing in air, which occurs under the picosecond regime, is not required. Consequently, NLC can be applied to large-aperture gratings to improve their laser damage resistance.

Acknowledgements

References

1. M. D. Perry, D. Pennington, B. C. Stuart, G. Tietbohl, J. A. Britten, C. Brown, S. Herman, B. Golick, M. Kartz, J. Miller, H. T. Powell, M. Vergino, and V. Yanovsky, Opt. Lett. **24**, 160 (1999).
2. L. J. Waxer, D. N. Maywar, J. H. Kelly, T. J. Kessler, B. E. Kruschwitz, S. J. Loucks, R. L. McCrory, D. D. Meyerhofer, S. F. B. Morse, C. Stoeckl, and J. D. Zuegel, Opt. Photonics News **16**, 30 (2005).

3. C. Radier, O. Chalus, M. Charbonneau, S. Thambirajah, G. Deschamps, S. David, J. Barbe, E. Etter, G. Matras, S. Ricaud, V. Leroux, C. Richards, F. Lureau, A. Baleanu, R. Banici, A. Gradinariu, C. Caldararu, C. Capiteanu, A. Naziru, B. Diaconescu, V. Iancu, R. Dabu, D. Ursescu, I. Dancus, C. A. Ur, K. A. Tanaka, and N. V. Zamfir, High Power Laser Sci. Eng. **10**, e21 (2022).

4. N. Blanchot, G. Behar, T. Berthier, B. Busserole, C. Chappuis, C. Damiens-Dupont, P. Garcia, F. Granet, C. Grosset-Grange, J. P. Goossens, L. Hilsz, F. Laborde, T. Lacombe, F. Laniesse, E. Lavastre, J. Luce, F. Macias, E. Mazataud, J. L. Miquel, J. Neauport, S. Noailles, P. Patelli, E. Perrot-Minot, C. Present, D. Raffestin, B. Remy, C. Rouyer, and D. Valla, EPJ Web Conf. **59**, 07001 (2013).

5. R. Tommasini, O. L. Landen, L. B. Hopkins, S. P. Hatchett, D. H. Kalantar, W. W. Hsing, D. A. Alessi, S. L. Ayers, S. D. Bhandarkar, M. W. Bowers, D. K. Bradley, A. D. Conder, J. M. Di Nicola, P. Di Nicola, L. Divol, D. Fittinghoff, G. Gururangan, G. N. Hall, M. Hamamoto, D. R. Hargrove, E. P. Hartouni, J. E. Heebner, S. I. Herriot, M. R. Hermann, J. P. Holder, D. M. Holunga, D. Homoelle, C. A. Iglesias, N. Izumi, A. J. Kemp, T. Kohut, J. J. Kroll, K. LaFortune, J. K. Lawson, R. Lowe-Webb, A. J. MacKinnon, D. Martinez, N. D. Masters, M. P. Mauldin, J. Milovich, A. Nikroo, J. K. Okui, J. Park, M. Prantil, L. J. Pelz, M. Schoff, R. Sigurdsson, P. L. Volegov, S. Vonhof, T. L. Zobrist, R. J. Wallace, C. F. Walters, P. Wegner, C. Widmayer, W. H. Williams, K. Youngblood, M. J. Edwards, and M. C. Herrmann, Phys. Rev. Lett. **125**, 155003 (2020).

6. S. P. Hatchett, C. G. Brown, T. E. Cowan, E. A. Henry, J. S. Johnson, M. H. Key, J. A. Koch, A. B. Langdon, B. F. Lasinski, R. W. Lee, A. J. Mackinnon, D. M. Pennington, M. D. Perry, T. W. Phillips, M. Roth, T. C. Sangster, M. S. Singh, R. A. Snavely, M. A. Stoyer, S. C. Wilks, and K. Yasuike, Phys. Plasmas **7**, 2076 (2000).

7. A. X. Li, C. Y. Qin, H. Zhang, S. Li, L. L. Fan, Q. S. Wang, T. J. Xu, N. W. Wang, L. H. Yu, Y. Xu, Y. Q. Liu, C. Wang, X. L. Wang, Z. X. Zhang, X. Y. Liu, P. L. Bai, Z. B. Gan, X. B. Zhang, X. B. Wang, C. Fan, Y. J. Sun, Y. H. Tang, B. Yao, X. Y. Liang, Y. X. Leng, B. F. Shen, L. L. Ji, R. X. Li, and Z. Z. Xu, High Power Laser Sci. Eng. **10**, e26 (2022).

8. H. Daido, M. Nishiuchi, and A. S. Pirozhkov, Rep. Prog. Phys. **75**, 056401 (2012).

9. D. Strickland and G. Mourou, Opt. Commun. **56**, 219 (1985).

10. Z. Chen, S. Zheng, X. Lu, X. Wang, Y. Cai, C. Wang, M. Zheng, Y. Ai, Y. Leng, S. Xu, and D. Fan, High Power Laser Sci. Eng. **10**, e32 (2022).

11. B. C. Stuart, M. D. Feit, S. Herman, A. M. Rubenchik, B. W. Shore, and M. D. Perry, J. Opt. Soc. Am. B **13**, 459 (1996).

12. J. A. Britten, W. A. Molander, A. M. Komashko, and C. P. J. Barty, Proc. SPIE **5273**, 1 (2004).

13. J. Neauport, E. Lavastre, G. Razé, G. Dupuy, and F. Desserouer, Opt. Express **15**, 12508 (2007).

14. N. Bonod and J. Néauport, Opt. Commun. **260**, 649 (2006).

15. J. Néauport and N. Bonod, Proc. SPIE **7132**, 71320D (2009).

16. L. Y. Xie, J. L. Zhang, Z. Y. Zhang, B. Ma, and X. B. Cheng, Opt. Express **29**, 2669 (2021).

17. B. Ashe, K. L. Marshall, C. Giacofei, A. L. Rigatti, T. J. Kessler, A. W. Schmid, J. B. Oliver, J. Keck, and A. Kozlov, Proc. SPIE **6403**, 64030O (2006).

18. B. Ashe, K. L. Marshall, D. Mastrosimone, and C. McAtee, Proc. SPIE **7069**, 706902 (2008).

19. B. Ashe, C. Giacofei, G. Myhre, and A. W. Schmid, Proc. SPIE **6720**, 67200N (2007).

20. H. T. Nguyen, C. C. Larson, and J. A. Britten, Proc. SPIE **7842**, 78421H (2010).

21. H. P. Howard, A. F. Aiello, J. G. Dressler, N. R. Edwards, T. J. Kessler, A. A. Kozlov, I. Manwaring, K. L. Marshall, J. B. Oliver, and S. Papernov, Appl. Opt. **52**, 1682 (2013).

22. N. Liu, R. Dent, B. N. Hoffman, A. A. Kozlov, J. B. Oliver, A. L. Rigatti, T. J. Kessler, S. G. Demos, and A. A. Shestopalov, Opt. Express **31**, 714 (2023).

23. J. Néauport, N. Bonod, and S. Hocquet, Proc. SPIE **8190**, 81900O (2011).

24. T. Liu, M. Zhu, W. Du, J. Shi, J. Sun, Y. Chai, and J. Shao, High Power Laser Sci. Eng. **10**, e30 (2022).

25. X. Zou, F. Y. Kong, Y. X. Jin, P. Chen, J. M. Chen, J. Xu, Y. L. Wang, Y. B. Zhang, and J. D. Shao, Opt. Mater. **91**, 177 (2019).

26. D. A. Alessi, C. W. Carr, R. P. Hackel, R. A. Negres, K. Stanion, J. E. Fair, D. A. Cross, J. Nissen, R. Luthi, G. Guss, J. A. Britten, W. H. Gourdin, and C. Haefner, Opt. Express **23**, 15532 (2015).

27. J. Xu, X. Zou, J. M. Chen, Y. B. Zhang, Y. L. Wang, Y. X. Jin, F. Y. Kong, H. C. Cao, P. Chen, and J. D. Shao, Opt. Lett. **44**, 2871 (2019).

28. H. Liddell, "Enhancing the performance of multilayer-dielectric diffraction gratings through cleaning process modifications and defect mitigation," PhD. Thesis (University of Rochester, 2014).

29. I. Jovanovic, C. G. Brown, B. C. Stuart, W. Molander, N. Nielsen, B. Wattellier, J. Britten, D. M. Pennington, and C. P. J. Barty, Proc. SPIE **5647**, 34 (2005).

30. X. K. Lin, Y. A. Zhao, X. F. Liu, D. W. Li, K. Shuai, H. Ma, Y. C. Shao, J. Sun, K. Q. Qiu, Y. Cui, Y. P. Dai, and J. D. Shao, Opt. Mater. Express **12**, 643 (2022).

31. S. Xu, X. Yuan, Y. Wei, X. Xia, and X. Zu, Opt. Mater. **31**, 1013 (2009).

32. M. Sahraee, H. R. Fallah, H. Zabolian, B. Moradi, and M. H. Mahmoodzade, Opt. Spectrosc. **118**, 627 (2015).

33. C. J. Stolz, L. M. Sheehan, S. M. Maricle, S. Schwartz, M. R. Kozlowski, R. T. Jennings, and J. Hue, Proc. SPIE **3264**, 105 (1998).

34. M. Kozlowski, Proc. SPIE **1438**, 143811 (1990).

35. H. Bercegol, Proc. SPIE **3578**, 421 (1998).

36. Y. N. Zhao, T. Wang, D. W. Zhang, J. Shao, and Z. Fan, Appl. Surf. Sci. **245**, 335 (2005).

37. J. Liu, X. Li, Z. K. Yu, H. Cui, W. L. Zhang, M. P. Zhu, and K. Yi, Proc. SPIE **8786**, 87860Z (2013).

38. Y. Zhao, J. Shao, T. Wang, D. Zhang, S. Fan, J. Huang, W. Gao, and Z. Fan, Proc. SPIE **5774**, 599 (2004).

39. X. K. Lin, Y. A. Zhao, X. F. Liu, D. W. Li, H. Ma, Y. C. Shao, K. Q. Qiu, J. Sun, F. Y. Kong, M. P. Zhu, and J. D. Shao, Proc. SPIE **11912**, 119120O (2021).

40. Y. Hao, M. Sun, S. Shi, X. Pan, Z. Zhu, X. Pang, and J. Zhu, Proc. SPIE **10339**, 103390H (2017).

41. K. Shuai, X. Liu, Y. Zhao, K. Qiu, D. Li, H. Gong, J. Sun, L. Zhou, Y. Jiang, Y. Dai, J. Shao, and Z. Xia, High Power Laser Sci. Eng. **10**, e42 (2022).

42. X. Cheng, J. Zhang, T. Ding, Z. Wei, H. Li, and Z. Wang, Light-Sci. Appl. **2**, e80 (2013).